Sub-size specimen testing for near-threshold fatigue crack behaviour of additively manufactured Ti-6Al-4V

Macallister, Nicolas; Chellu, Sreyas; Riemslag, Ton; Scott, Sean Paul; Ayas, Can; Popovich, Vera; Becker, Thorsten Hermann

DOI
10.1016/j.mtla.2023.101852

Publication date
2023

Document Version
Final published version

Published in
Materialia

Citation (APA)
Macallister, N., Chellu, S., Riemslag, T., Scott, S. P., Ayas, C., Popovich, V., & Becker, T. H. (2023). Sub-size specimen testing for near-threshold fatigue crack behaviour of additively manufactured Ti-6Al-4V. *Materialia*, *30*, Article 101852. https://doi.org/10.1016/j.mtla.2023.101852

MTLA 30 (2023) 101852

Contents lists available at ScienceDirect

Materialia

journal homepage: www.elsevier.com/locate/mtla

Full Length Article

Sub-size specimen testing for near-threshold fatigue crack behaviour of additively manufactured Ti-6Al-4V

Nicolas Macallister [a,*], Sreyas Chellu [b], Ton Riemslag [b], Sean Paul Scott [b], Can Ayas [c], Vera Popovich [b], Thorsten Hermann Becker [d]

[a] Department of Mechanical and Mechatronic Engineering, Stellenbosch University, Joubert street, Stellenbosch 7602, South Africa
[b] Department of Materials Science and Engineering, Delft University of Technology, Mekelweg 2, Delft, CD 2628, the Netherlands
[c] Department of Precision and Microsystems Engineering, Delft University of Technology, Mekelweg 2, Delft, CD 2628, the Netherlands
[d] Centre for Materials Engineering, University of Cape Town, Library Rd, Cape Town 7701, South Africa

ARTICLE INFO

Keywords:
Additive manufacturing
Ti-6Al-4V
Sub-size specimen
Fatigue strength
Near-threshold fatigue crack growth, Crack tip constraint

ABSTRACT

Sub-size specimen testing offers a potentially elegant solution to accompany fatigue life assessments in determining vital fatigue parameters such as effective fatigue crack growth propagation thresholds ($\Delta K_{th,eff}$). Additively manufactured parts stand to benefit from this in potential build-by-build fatigue validation without foregoing process-inherent material saving and low lead times. In this study, sub-size Laser Powder Bed Fusion (LPBF) produced Ti-6Al-4 V SENB specimens built in two orientations with stress relieved and annealed material states are considered. Scanning electron microscopy with electron backscatter diffraction is used to consider both meso- and microstructural features, complimented by digital image correlation (DIC) for determining local stress intensity and triaxiality around the crack tip. Results show inconsistent near-threshold fatigue behaviour linked to the microstructure of annealed material, where the fatigue threshold in sub-size specimens is reduced. Furthermore, reducing specimen size influences both in- and out-of-plane crack tip constraint, with higher constraint experienced by the sub-size specimens. Overall, this study presents and discusses the domain and suitability in using sub-size specimen FCGR threshold testing for LPBF produced Ti-6Al-4 V builds considering their unique meso- and microstructural features.

1. Introduction

Additive manufacturing (AM), as opposed to conventional ‘subtractive’ manufacturing, is moving towards wide adopted in industry due to the inherent manufacturing benefits in increased build complexity, low lead times and reduced material cost [1]. Laser Powder Bed Fusion (LPBF) is amongst the most popular AM techniques for aerospace, automotive and biomedical application due to its relatively higher resolution and accuracy [2]. This has led to an essential research drive in understanding mechanical properties and reliability of AM-produced components [3], where the Ti-6Al-4 V alloy has been a focus due to its popularity in aerospace and biomedical applications for its lightweight and high strength mechanical properties [4]. Furthermore, static properties of as-fabricated LPBF Ti-6Al-4 V are shown to be comparable to conventional material, and with additional novel post-process treatments, may reach similar dynamic properties [5–7].

Of the remaining challenges to LPBF produced Ti-6Al-4 V and generally AM parts, the qualification and certification of mechanical properties requires further development [1]. AM-inherent attributes such as surface asperities, void type flaws, residual stresses and spatial variations in the microstructure (linked to build orientation and location) affect mechanical behaviour of LPBF produced components [1, 7–9] in symphony creating uncertainty in the material behaviour, which reduces the advantages of AM and inhibits its integration into safety-critical applications. The relationship of these effects coupled with build-to-build and machine-to-machine variability leads to the necessity for more reliable certification avenues [1]. Although there is considerable investigation on aspects of the manufacturing process, tensile properties, and microstructure, fatigue and fracture performance require greater depth of research [1]. As many safety-critical applications experience a degree of cyclic loading, understanding these fatigue properties is a critical aspect in design. Thus, the relationship between fatigue and the process-inherent attributes in AM components has resulted in formulation of damage tolerant design philosophies wherein unique build-by-build material characteristics, such as inherent void

* Corresponding authors.
E-mail address: 19009143@sun.ac.za (N. Macallister).

https://doi.org/10.1016/j.mtla.2023.101852
Received 12 May 2023; Accepted 12 July 2023
Available online 13 July 2023

Nomenclature

Abbreviation

AM	additive manufacturing/manufactured
AN	annealed
FCGR	fatigue crack growth rate
LEFM	linear elastic fracture mechanics
LPBF	laser powder bed fusion
PBG	prior beta grain
SR	stress relief

Symbol

a	crack length
ΔK	stress intensity factor range
ΔK_{th}	fatigue crack growth rate threshold
$\Delta K_{th,eff}$	effective fatigue crack growth rate threshold
$\Delta K_{th,lc}$	long crack growth rate threshold (R dependant)
α	material three-dimensional stress constraint
σ_u	ultimate tensile strength
σ_{ys}	Yield strength
E	Young's modulus
$\frac{da}{dN}$	fatigue crack growth rate
d_{10}	10th percentile of powder particle size distribution
d_{50}	50th percentile of powder particle size distribution
d_{90}	90th percentile of powder particle size distribution
κ	Kosolovs' constant
R	load ratio
K_I	mode I opening plain strain stress intensity factor
K_{II}	mode II plain strain stress intensity factor
r_p	cyclic plastic zone size
μ	shear modulus
ν	Poissons ratio

type defects, surface asperities and microstructures, are incorporated as part of the fatigue life predictions [10]. Typical modelling approaches use descriptions of fatigue crack growth (FCR) through modification of classical fracture mechanics as a foundation and estimate a component life indicator based on knowledge of the AM-inherent microstructures and defect structure descriptions. Furthermore, many existing works include the Kitigawa Takahashi (KT) methodology for marrying the FCG and traditional stress-based approaches into a useful visualisation of acceptable stress levels for practical design [11]. Conventionally the double-logarithmic KT plot correlates governing crack size to a corresponding cyclic fatigue limit where crack growth will arrest [12].

However, the applicability of damage tolerant models completely independent of destructive material testing is still non-feasible as many of these models contain considerable amounts of parameters derived from prior bulk mechanical testing. Therefore, the usefulness and accuracy of resulting design approaches, such as KT depictions, may not capture build-specific fatigue behaviour. To this extent, one of the most important parameters in describing FCG is the value of the fatigue crack growth threshold (ΔK_{th}), which Macallister and Becker [10] demonstrated as a sensitive material property for the resulting model estimated fatigue life. Knowledge of ΔK_{th} is essential, as it denotes the location where FCG is assumed to cease or become low enough to be neglected [13]. Furthermore, ΔK_{th}, along with initial defect size (a), are dominant descriptors of the near-threshold behaviour which is considered to consume a majority of component fatigue life and is sensitive to the unique microstructural features of LPBF produced Ti-6Al-4 V [5,14]. ΔK_{th} may further be split into $\Delta K_{th,lc}$ and $\Delta K_{th,eff}$ values representative of the long crack growth FCG threshold and the closure-free effective FCG threshold respectively. Crack closure phenomena in long crack growth act as a crack tip shielding mechanism, retarding the crack driving force through premature contact of crack faces during the loading cycle. Reported in three possible mechanisms, namely: plasticity, roughness, and oxide-induced closure [15]. In general application the severity of the crack closure is dependant on the material and load ratio (R), with lower R values and material with higher flow properties experiencing relatively higher degrees of crack closure, which contributes to higher measured $\Delta K_{th,lc}$ values. However, these effects are typically assumed to subside at higher R values where the crack is considered fully open through the cycle and contact shielding therefore is unlikely to occur in the wake. Conversely, $\Delta K_{th,eff}$ values are considered as a material property independent of loading and can be expanded in combination with plasticity induced, roughness induced and oxide induced descriptions [15] to capture $\Delta K_{th,lc}$ at other loading conditions. In previous work [5], this was successfully demonstrated for LPBF Ti-6Al-4V. Therefore, the value of $\Delta K_{th,eff}$ forms a keystone parameter for damage tolerant assessments.

To this end, a potentially elegant solution to accompany fatigue life assessments and determine parameters such as $\Delta K_{th,eff}$ resides in the use of limited material sub-size specimen testing accompanying AM built components. Historically introduced and used by the nuclear industry for characterising in- and post service irradiated material characteristics [16], sub-size specimen testing has since evolved with the emergence of new high-performance materials and technologies [17] where the technique is typically used for evaluation of component material performance characteristics during service, without compromising the structure of interest [18]. In application to AM, extracting material properties from sub-size specimen on a build-by-build basis without foregoing the benefits inherent to LPBF has garnered significant interest [19]. Furthermore, sub-size specimens inherently enable extraction of material specimens in component critical loading regions, helping to address the problem of similitude or transferability between the material specimen and built component [12]. While significant research exists on sub-size specimen testing for tensile [20–22] and stress-life fatigue properties [23], validity of sub-size specimens for FCR rate characterisation in AM materials is less defined and standardisation efforts remain in a formative stage [12]. This work aims to extend and define the current domain and suitability in using sub-size specimen FCGR threshold testing for LPBF produced Ti-6Al-4V builds. Here, consideration to the unique meso- and microstructure of the material, crack tip constraint, suitability, and limitations are discussed.

2. Materials and methods

2.1. Specimen fabrication

LPBF produced specimens were fabricated in a facility[1] certified with ISO 9001 and ISO 13,485 using an EOSINT M280 LPBF machine, with Ti-6Al-4 V gas atomised powder both supplied by EOS (GmbH, Krailling, Germany). The powder was measured to have a chemical composition of 6.47% Al, 4.22% V, 0.22% Fe, 0.01% N, 0.07% O_2 and the balance Ti with a particle size distribution of $d_{10} = 28$ μm, $d_{50} = 47$ μm and $d_{90} = 71$ μm. The chemical composition of the powder lot was in accordance with the limits defined by the ASTM F3001 [24] material specification. Printing parameters implemented are presented in Table 1. Argon gas was used to flood the building chamber, and the oxygen level was maintained below 0.12% during the fabrication process. Individual

[1] The Centre for Rapid Prototyping and Manufacturing (CRPM) at the Central University of Technology located in South Africa.

Table 1
L-PBF printing parameters.

Power (W)	Scan Speed (mm/s)	Layer Thickness (μm)	Laser Spot Diameter (μm)	Hatch Spacing (μm)	Energy Density (J/mm^3)
170	1200	30	80	100	47

SENB specimens were printed in a near-net shape at similar height with scans in a stripe pattern of 5 mm length and a scan rotation of 67 between each layer. Further receiving a stress relief (SR) while attached to base plate at 610 °C for 1 h followed by air cooling.

Specimens were printed in two build orientations, namely XZY and YXZ according to ISO/ASTM52921:2017, hereafter referred to as *Flat* and *Vertical* as presented in Fig. 1. Furthermore, at two size scales, hereafter referred to as *large* and *small*, where the small group denotes the sub-sized specimens. The final dimensions, as designated by BS ISO 12,108:2018, were W = 10 mm & B = 5 mm, and W = 5 mm & B = 2.5 mm for the *large* and *small* specimens respectively. A third of the specimens received a further anneal of 920 °C for 2 h in vacuum followed by a furnace cool of 4 °C/min, in line with authors prior work for the annealed (AN) condition [6]. As a final step, all specimens were milled to final dimensions, removing approximately 1 mm of material and therefore any α case hardening that formed during the heat treatment from all sides, and starter notches were subsequently wire-cut using electrical discharge machining (EDM). Final polishing of specimen side surfaces was conducted to aid in visual crack measurement during testing.

2.2. Specimen analysis

Microstructural analysis was performed on sectioned, polished and etched (Kroll's reagent: 100 ml of distilled water + 6 ml of nitric acid + 3 ml HF) specimens, around the crack tip of the SR and AN specimens. Both scanning electron microstructural (SEM) and fractographic analyses were performed using a Jeol JSM IT-100 (JEOL, Tokyo, Japan) in conjunction with a backscatter detector. X-ray diffraction (XRD) for estimating phase fractions in the microstructure was analysed on a Bruker D8 Advance diffractometer with Bragg- Brentano geometry and Lynxeye detector. Detection used a Cu Kα radiation of 45 kV and 40 mA. For meso- structural PBG reconstruction, alpha grain size distribution and texture analysis electron backscatter diffraction (EBSD) scans were performed using a Tescan MIRA 3 Advanced with Oxford Instruments Nordlys detector and Aztec 6.0 software. The EBSD was analysed using the MTEX toolbox available for MATLAB [25], where the angle of misorientation threshold for the alpha grain reconstruction was selected as 10° and the measurement of the grain size distribution was performed according to the linear intercept method [26,27]. Furthermore, hardness measurements were obtained with a Struers Durascan at load 0.3 Kgf and 15 second dwell on the plane perpendicular to fatigue loading.

2.3. Near-threshold fatigue testing

Near-threshold FCGR testing was conducted on a MTS servo-hydraulic testing machine fitted with a 25 kN load cell and operated using the MTS MultiPurpose TestWare and FlexTest electronic unit [28, 29]. Testing was conducted in ambient laboratory conditions using sinusoidal test frequencies of 60–70 Hz. A minimum of three samples per group were tested with a constant K_{max} load shedding technique accompanied by a direct current potential drop (DCPD) technique for crack length monitoring as per ASTM E647 [30]. The DCPD was experimentally calibrated for each specimen during the fatigue pre-cracking phase with aid of two Limess digital image correlation (DIC) cameras mounted either side of the specimen monitoring the visual crack length against known lengths scribed on the specimen surfaces. K_{max} was held at 14.5 MPa$\sqrt{\text{m}}$, whereas K_{min} was increased, according to a load shedding gradient of -0.095 m^{-1} to accommodate small scale yielding (SSY) requirement in the *small* specimens. R was started in the region of 0.5 to 0.65 and increased through the test, typically completing in the region between 0.8 and 0.9. Near-threshold FCG rate data was processed in MATLAB. When necessary, correction was made for the experimental DCPD calibration from the visual crack measurements during the test and the post-mortem microscope measurement of the crack length. Processing included smoothing response data using a 5% moving average filter with coefficients determined by unweighted linear least-squares regression and a second order polynomial model. ΔK_{th} was determined from linear regression of da/dN data points between 10^{-7}–10^{-8} mm/cycle.

2.4. Crack tip displacement field fitting

Stress intensity factor range (ΔK) and cyclic T-stress (ΔT-stress) values were determined using a field fitting approach to experimental displacement fields around the crack tip, matched to a Williams' asymptotic formulation [31]. Displacement fields were captured and correlated using digital image correlation (DIC), in line with the measurement guidelines outlined in [32]. A Limess system fitted with 5-megapixel camera and telecentric lens (TC 23,036, Opto-engineering) was used for acquisition. A speckle pattern was applied with an aerosol spray and the system calibrated through linear scaling from known distances. Furthermore, LaVision Davis 8 correlation software with subset and step size of 47 and 5 pixels respectively was selected for the correlation through a 2nd order subset shape function, with one pixel length representing ~7 µm. Experimental images were captured at a constant K_{max} of 15.5 MPa$\sqrt{\text{m}}$ with an image rate of 10 Hz while the test cycling frequency was set at 1 Hz. To create a range of ΔK values, repeat tests were done at R selected at 0.1, 0.5 and 0.8 (independent to threshold testing) with a similar crack length such that only the force values were changed.

The displacement fields surrounding crack tip were assumed to fit a mixed mode I and II condition such that the field can be approximated from the Williams formulation as per the Williams' form used by Yates *et al.* [33], using

$$\text{Mode I} \begin{cases} u_I = \sum_{n=1}^{\infty} \frac{r^{\frac{n}{2}}}{2\mu} a_n \left\{ \left[\kappa + \frac{n}{2} + (-1)^n \right] cos\frac{n\theta}{2} - \frac{n}{2} cos\frac{(n-4)\theta}{2} \right\} \\ v_I = \sum_{n=1}^{\infty} \frac{r^{\frac{n}{2}}}{2\mu} a_n \left\{ \left[\kappa - \frac{n}{2} - (-1)^n \right] sin\frac{n\theta}{2} + \frac{n}{2} sin\frac{(n-4)\theta}{2} \right\} \end{cases} \tag{1}$$

and,

$$\text{Mode II} \begin{cases} u_{II} = -\sum_{n=1}^{\infty} \frac{r^{\frac{n}{2}}}{2\mu} b_n \left\{ \left[\kappa + \frac{n}{2} - (-1)^n \right] sin\frac{n\theta}{2} - \frac{n}{2} sin\frac{(n-4)\theta}{2} \right\} \\ v_{II} = \sum_{n=1}^{\infty} \frac{r^{\frac{n}{2}}}{2\mu} b_n \left\{ \left[\kappa - \frac{n}{2} + (-1)^n \right] cos\frac{n\theta}{2} + \frac{n}{2} cos\frac{(n-4)\theta}{2} \right\} \end{cases} \tag{2}$$

Here, u and v denote the mode I and II displacements in the horizontal and vertical directions, κ Kolosovs constant and μ the shear modulus respectively. Furthermore, κ and μ are formulated in terms of E and ν as $= E/2(1+\nu)$ and $\kappa = (3-\nu)/(1+\nu)$ respectively for a state of plane stress at the specimen surface. Values for E were selected as from prior work on AN and SR LPBF Ti-6Al-4 V material as 114 and 116 *GPa* [34] and ν held at a constant 0.3. The form of Williams functions in Eqs. (1) and (2), with a minimum of 10 terms to ensure accurate stress intensity factor solutions [35], was solved in combination with the crack tip location from an estimated position as a non-linear least squares problem [36–38]; increasing the number of higher order terms has been suggested to improve accuracy of solutions when using larger displacement fields [39]. The minimisation between experimental and analytical displacement data solver was implemented in a non-linear least squares solver based on the Levenberg-Marquardt algorithm

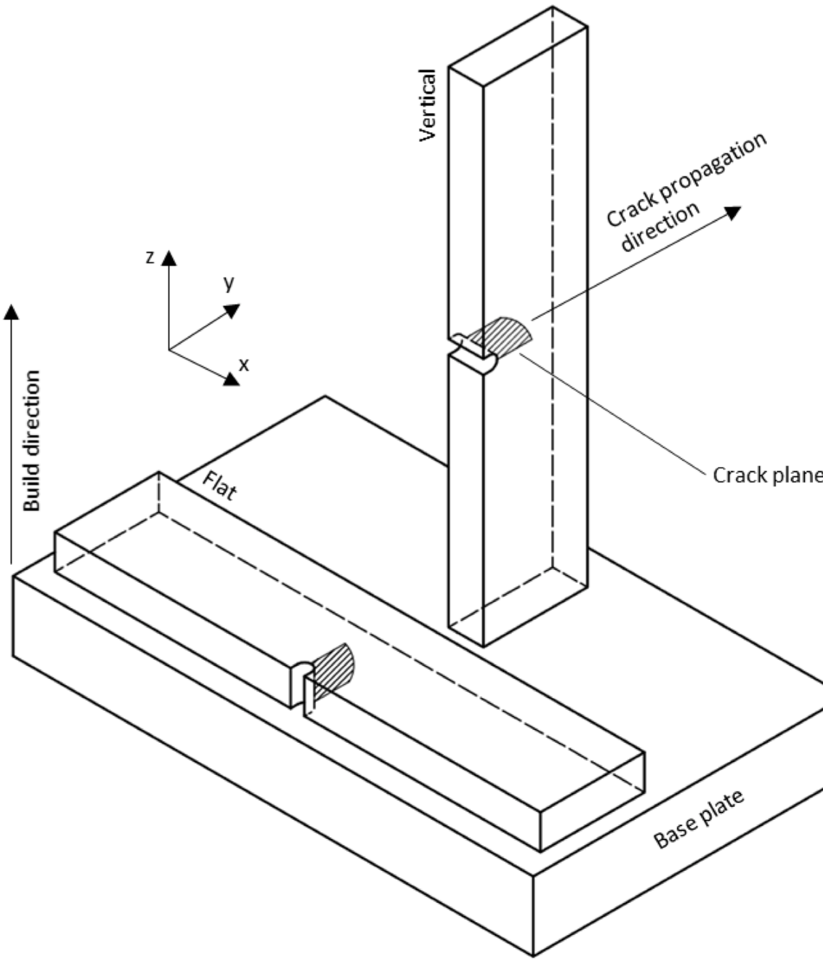

Fig. 1. Specimen build orientations, crack planes and crack propagation direction.

available in MATLAB R2022b.

3. Results

3.1. Microstructure

The microstructure for LPBF produced Ti-6Al-4 V is presented in Fig. 2a and b for the SR and AN material state respectively. Fig. 2a presents the typical acicular needle-shaped grain structure consisting of predominantly single-phase metastable α' [6,40] of as-fabricated material with partial decomposition to acicular α from the SR. The acicular needle structure is observable in detailed view in Fig. 2a. Following the high solid-solution temperature AN, the α' microstructure is decomposed into lamella α with laths of width 2–5 µm (Fig. 2b). Furthermore, phase fractions measured by XRD indicate an increase in β from 3.5 to 7.1% after AN (Fig. 3), where around a 2θ angle of 39° small peaks in the

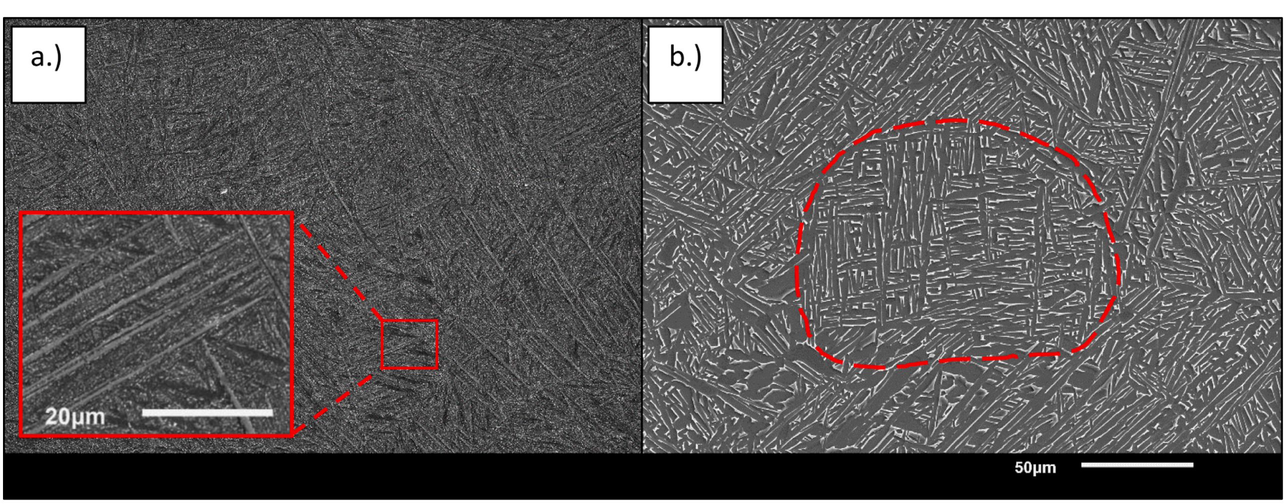

Fig. 2. Micrographs of (a) SR and, (b) AN material in the XY plane.

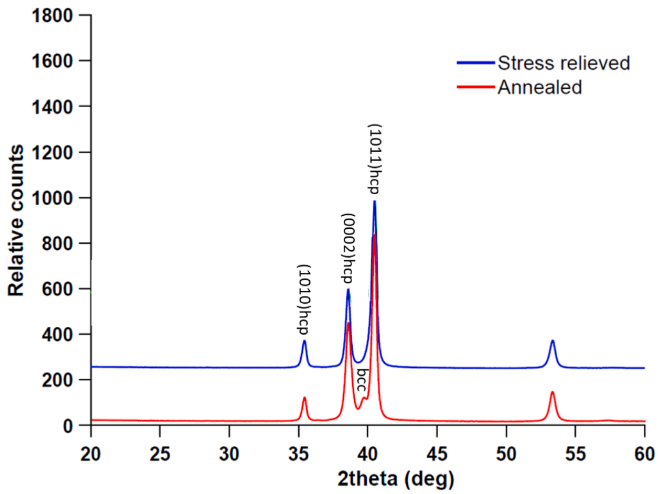

Fig. 3. XRD analysis of AN and SR material.

AN sample corresponds to the β phase quantified though Rietveld fitting [41]; the higher temperature of the AN result in increased nucleation of β phase along α grain boundaries. Previous studies link improved tensile elongation and fatigue properties to the increased presence of ductile β phase in the high solid-solution temperature region [42,43]. However, this comes with a trade-off between a lower YS and UTS but an increase in ductility [34,44]. The results of the microhardness test presented in Table 2 are indicative of this decrease in tensile strength and increased ductility through the well-known Hall-Petch phenomenon; the increase in grain size correlates with the decrease in hardness [45].

Furthermore, the description of LPBF produced Ti-6Al-4 V is incomplete without mentioning reported mesostructural prior-beta grain (PBG) features [7,46]. Indicated by the dashed line in Fig. 2b, PBGs form due to the thermal gradients and cooling rates, presenting in elongated columnar structures parallel to build direction [40,47]. These PBG structures are suggested to remain stable post-solidification and do not change under heat treatments below beta-transus temperature [40], meaning the structure is consistent in both SR and AN material state.

3.2. Near-threshold FCG rate behaviour

The near-threshold FCG rates are presented in Fig. 4 grouped together by material state (Fig. 4a and b) and orientation (Fig. 4 c). Each data set represents the combination of test repeats per orientation, with the shaded areas representing the 95% confidence interval on linear least squares fits to FCG rates between 10^{-7}–10^{-8} mm/cycle, representing the $\Delta K_{th,eff}$ range. It was found that *large* and *small* LPBF produced Ti-6Al-4 V specimens in the SR state were comparable (Fig. 4a) with both $\Delta K_{th,eff}$ values found in the range centred around 1.83 ± 0.1 MPa$\sqrt{\mathrm{m}}$. However, for AN material (Fig. 4b) the $\Delta K_{th,eff}$ values for *small* specimens decreased by ~19% from 2.66 ± 0.2 to 2.13 ± 0.2 $MPa\sqrt{m}$ from the *large* to the *small* specimens respectively, indicating a size effect unique to the AN microstructure. These results are further detailed in Table 2. Furthermore, the values reported in the SR material state for the *small flat* specimens (1.55 ± 0.1 $MPa\sqrt{m}$) and *small vertical* (1.85 ± 0.15 $MPa\sqrt{m}$) specimens are presented (Fig. 4c) and are congruent with full scale LPBF produced Ti-6Al-4 V specimens in a SR material state as previously reported [1]. To note, two tests were performed at a higher K_{max} value (17 $MPa\sqrt{m}$) to rule out possible effects on $\Delta K_{th,eff}$. Lower values of K_{max} have been reported to lead to overestimation of $\Delta K_{th,eff}$ values [47], however here as both K_{max} values result in similar $\Delta K_{th,eff}$ its effects are considered negligible. The difference in orientation effect on $\Delta K_{th,eff}$ between vertical and horizontal specimens has been attributed to different meso-structural PBG structures [47]. Therefore, we suggest the consistency between these two independent studies for orientational $\Delta K_{th,eff}$ values of LPBF produced Ti-6Al-4 V likely means meso- structural features and build orientation do not influence $\Delta K_{th,eff}$ values determined for the sub-size specimens investigated here.

For all tests we observe an increased scatter at lower growth rates; this is likely due to the stability of the DCPD system, whereby the resolution of the crack monitoring is reduced as the FCGR decreases, and small perturbations caused by noise or irregularities in the signal are more pronounced. Simply, the difference in voltage required to estimate crack growth in the threshold regime according to the calibration equation approaches the system signals' natural noise as the FCG rate decreases, resulting in increasingly scattered points.

3.3. Fractographic analysis

With reference to Figs. 5 and 6 we observe the fatigue fracture path through the different material states and size specimens. For the SR material (Fig. 5) the cracks exhibit propagation in mixed mechanism trans- and intergranular growth, where intergranular growth occurs along the α' grain boundaries, denoted by the sudden change in growth direction. Intergranular boundary growth has been suggested to occur from a more energetically favourable crack path where a higher dislocation density along α' grain boundaries is formed through high cooling rates in the LPBF process [48]. Furthermore, brittle α' has been suggested to weaken grain boundaries, making them more favourable for cracks to traverse.

Conversely, for the AN material (Fig. 6) the crack mechanism changes to dominantly transgranular growth as the brittle α' grains are decomposed into a α+β phase and the grain boundary weakening effect is mitigated [34]. Consistent fracture mechanism behaviour is observed in both materials for *large* and *small* sample groups. Notably, for the AN material more bifurcations are present along the crack path of the *small* specimen group relative to the *large.* This secondary cracking may be due to a higher energy state in the sub-size specimens, which dissipates by branching to secondary crack planes. When the crack tip energy has been dissipated, the branched secondary crack stops growing and the primary crack on the primary crack plane, which is the plane of loading, continues growing.

3.4. Fitted stress intensity factor value

Local ΔK values around the crack tip for vertical specimens in each material state and size as per the field fitting technique (Section 2.4) are compared to those theoretically applied as per standard empirical equations ASTM E399 [49] for a SENB configuration. Fig. 7

Table 2
FCG rate testing results.

Material state	Group	Orientation	Hardness ($HV_{0.3}$)	R	$\Delta K_{th,eff}$ ($MPa\sqrt{m}$)	K_{max} ($MPa\sqrt{m}$)
SR	*large*	vertical	394 ±9	0.88	1.83 ±0.1	14.5
	small	vertical	396 ±9	0.88	1.85 ±0.2	14.5, 17
		flat		0.9	1.55 ±0.1	14.5
AN	*large*	vertical	345 ±14	0.82	2.66 ±0.2	14.5
	small	vertical	351 ±12	0.86	2.13 ±0.2	14.5, 17

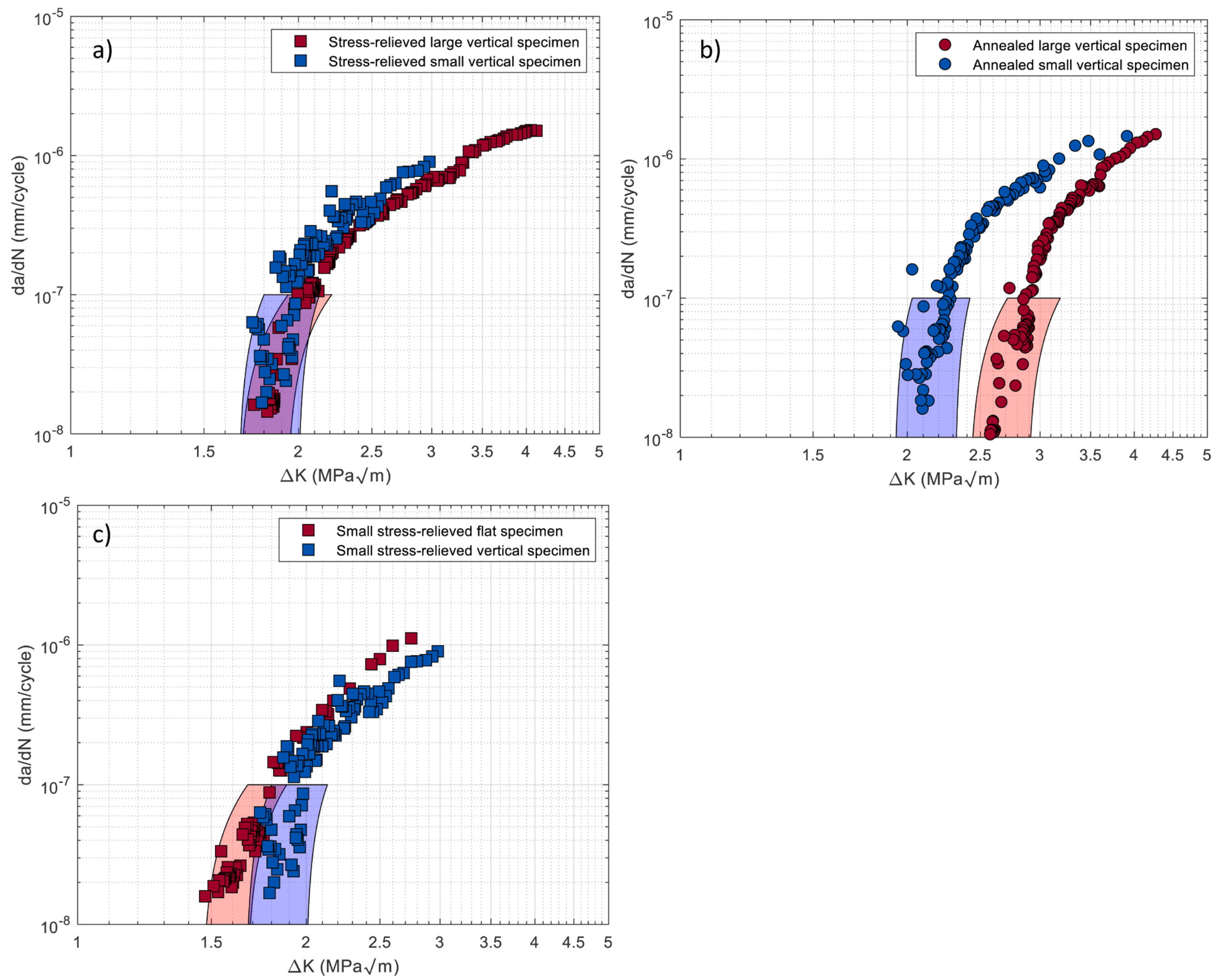

Fig. 4. Near-threshold FCG rates in (a) SR vertical, (b) AN vertical and (c) SR vertical and flat orientation.

demonstrates the fitting procedure and resulting fits, where Fig. 7a shows the initial selection of crack tip and crack area for fitting, and Fig. 7b the optimisation results at incremental increasing of higher order terms in the Williams series for K_I and K_{II}.

Here K_I represents ΔK for the application of this study as K_{min} was taken as the reference. Finally, Fig. 7c and d illustrate the contours of experimentally measured displacement fields (dashed) against fitted (solid) as used for visual validation of the method. For the analysis the crack region is masked, creating the discontinuity in fitted contours in Fig. 7c and d. Typically this masking is applied to prevent the nonphysical imaged data across the cracked region introducing errors in analysis from incorrect matching between subsets in the DIC algorithm. Notably, extracted K_I values have been shown to be relatively unaffected by this procedure in mode I loading [50], and the use of a full field fitting approaches remain accurate under the assumption of a continuous material.

Fig. 8 presents these results for SR and AN material respectively, with the dashed line representing the case where the applied ΔK is congruent to the measured ΔK. In both cases the *small* specimen local measured ΔK values are higher than that of the *large* specimens indicated by the vertical spacing between red and blue markers, with the AN materials deviation more exaggerated between sizes. Furthermore, typically this difference is more pronounced for higher ΔK applied values (Fig. 8). Detailed results are further presented in Table 3. The difference at higher ΔK is likely in part related to a more significant contribution of the crack closure phenomena linked to lower R. Qualitatively, the larger crack face area within the *large* specimen group creates more potential for contact shielding from crack face asperities (roughness induced closure) at low R, which has been suggested to appear in LPBF produced Ti-6Al-4 V. However, $\Delta K_{th,eff}$ values are representative of a closure free state at high R (low $\Delta K_{applied}$) where the discrepancy of measured effective ΔK between specimen sizes is unaccounted for.

4. Discussion

4.1. Influence of meso- and microstructure on fatigue behaviour

The near-threshold FCG behaviour of LPBF produced Ti-6Al-4 V has been closely linked to the influence of material meso- and microstructural characteristics [51]. The *Large* SR specimens demonstrate a lower $\Delta K_{th,eff}$ compared to AN material. Firstly, considering the effect of plasticity, SR microstructure contains predominantly brittle phase α' and some amounts of α- and β-phase; the brittle nature of α' suggests relatively higher values of yield stress (σ_y), and a reduced plastic zone size formed in front of the crack tip. This can be idealised using Eq. (3) under a small scale yielding (SSY) assumption [52], using

$$r_p = \frac{1}{6\pi}\left(\frac{K_{max}}{\sigma_y}\right)^2 \tag{3}$$

Where, K_{max} relates to the maximum stress intensity factor experienced during cyclic loading. In a previous study by the author [6], σ_y values

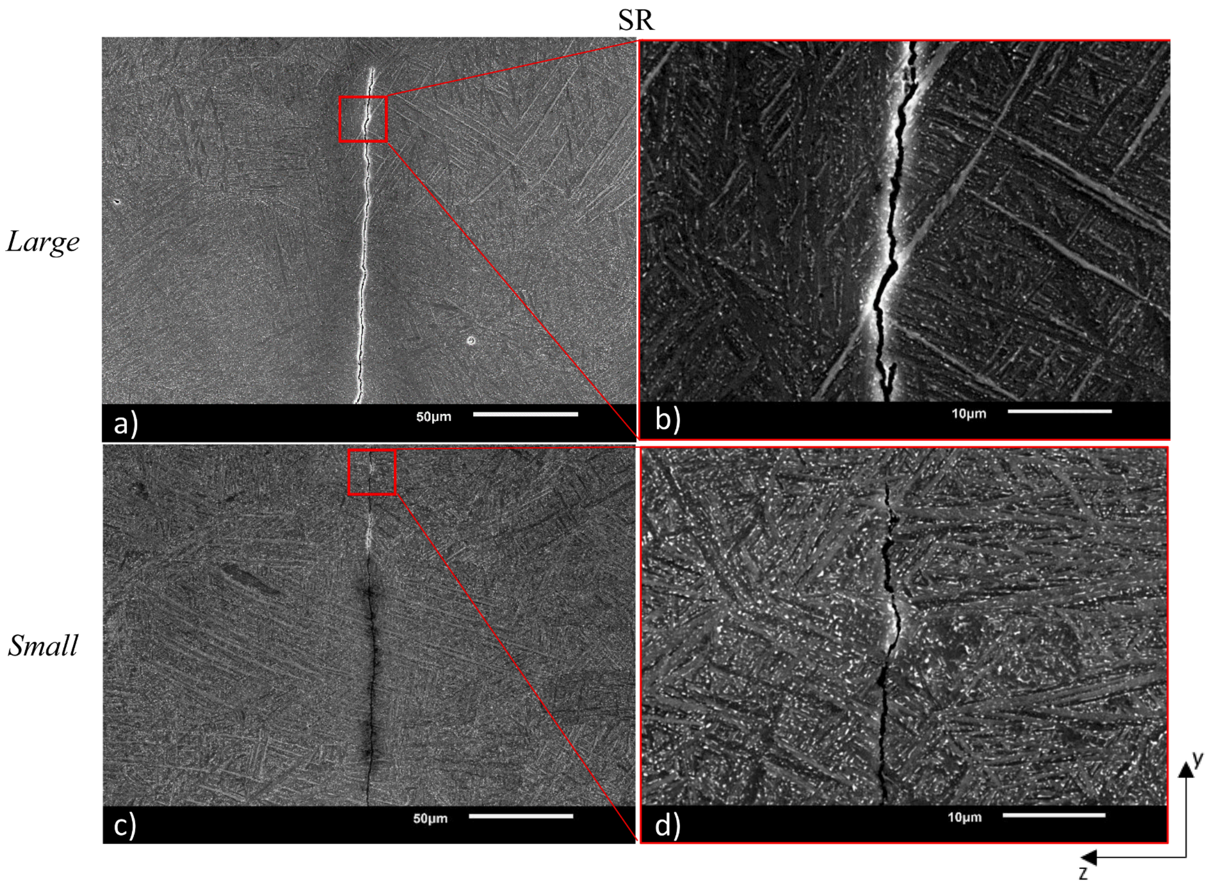

Fig. 5. FCG through SR microstructure in the near threshold regime. With a & b large, and c & d small specimen groups (b and d presenting respective detailed views.).

were determined as 870 and 1035 MPa for AN and SR respectively. The smaller plastic zone size for SR material (~10 μm) in turn leads to lower energy dissipation at the crack tip through plastic work, and lower values of ΔK are reached before input energy is balanced by plastic work and crack propagation ceases at ΔK_{th}. Comparatively, AN material has a coarser microstructure with α laths which are greater in thickness and have larger fractions of ductile β-phase at the grain boundaries. The larger fraction of ductile β-phase in the AN material conveys lower values of σ_y and a larger plastic zone size (~14 μm) ahead of the crack tip (Eq. (3)). Therefore, more energy is dissipated through plastic work and ΔK_{th} values which are relatively higher than those of the SR material result.

Qualitatively, the impedance to crack growth is dependant on the crack tortuosity, where Kumar et al. [7] proposed an influence by microstructural features in the same length scale as r_p, becoming more pronounced in the near-threshold regime (where r_p is at minimum). Similarly, Sadananda and Ramaswamy [53] quantified this relation in Ti alloys to r_p ~1.5l for a discernible influence, where l represents the size of the microstructural feature. This lends to explaining the observed orientational difference between SR small samples (Fig. 4c) where different build orientations are suggested to lead to greater or lesser crack tortuosity incurred by crack deflection along the larger length scale meso-structural PBGs [5,47].

Fig. 9 presents the crack propagation through reconstructed PBGs and α grain size distributions for the *large* and *small* AN specimens, captured around the crack tip in the near-threshold region of growth. First, we examine the crack profile through the PBG structure (Fig. 9a and b), where the crack path propagates through the PBG grain structure observed for both the *small* and the *large* and is not significantly deflected. Second, the α grain size distribution between sample sizes shows a slight decrease (by ~ 10%) in grain size for the *small* AN group. Rasavi et al. [54] observed this effect of reduced specimen size resulting in finer grains for thinner specimens in EBM produced Ti-6Al-4 V, where faster cooling rates were suggested in the thinner specimens compared to the larger group, which was capable of dissipating heat through the cross section slower [54]. This in turn showed an influence on reduced ductility for thinner samples [54], which in the context of FCG rates would suggest a reduced r_p. However, the influence of this measurement between the *large* and *small* specimen $\Delta K_{th,eff}$ for AN material is questionable, as firstly the cooling rate for the AN heat treatment was likely slow enough to mitigate this effect: ~4 °C/min for a typical furnace cool [55]. Furthermore, the $\Delta K_{th,eff}$ values for SR material, where the difference in cooling rates would be more pronounced between specimen sizes, are similar (Fig. 4a), suggesting the potential effect of grain refinement for smaller thicknesses in the geometries investigated in AN is unlikely.

It should be noted that this morphological effect may change as the size of the specimen is further reduced and is important to measure and consider when reporting $\Delta K_{th,eff}$ values for damage tolerant design model frameworks.

The sensitivity of the link between near-threshold FCG behaviour in LPBF produced Ti-6Al-4 V has been well established by Kumar et al. [7, 14] and Becker et al. [1], where Burns *et al* [56] describes the critical mechanisms of the microstructure on FCG as the local tortuosity of the primary crack path and the propensity to develop secondary cracking. In this regard, morphologically the relative differences in the AN microstructures between *large* and *small* specimens suggest no significant difference. However, observably crack propagation in the *small* AN configuration demonstrates more secondary cracking (as indicated by the arrows in Fig. 6c). This suggests the AN microstructure is more

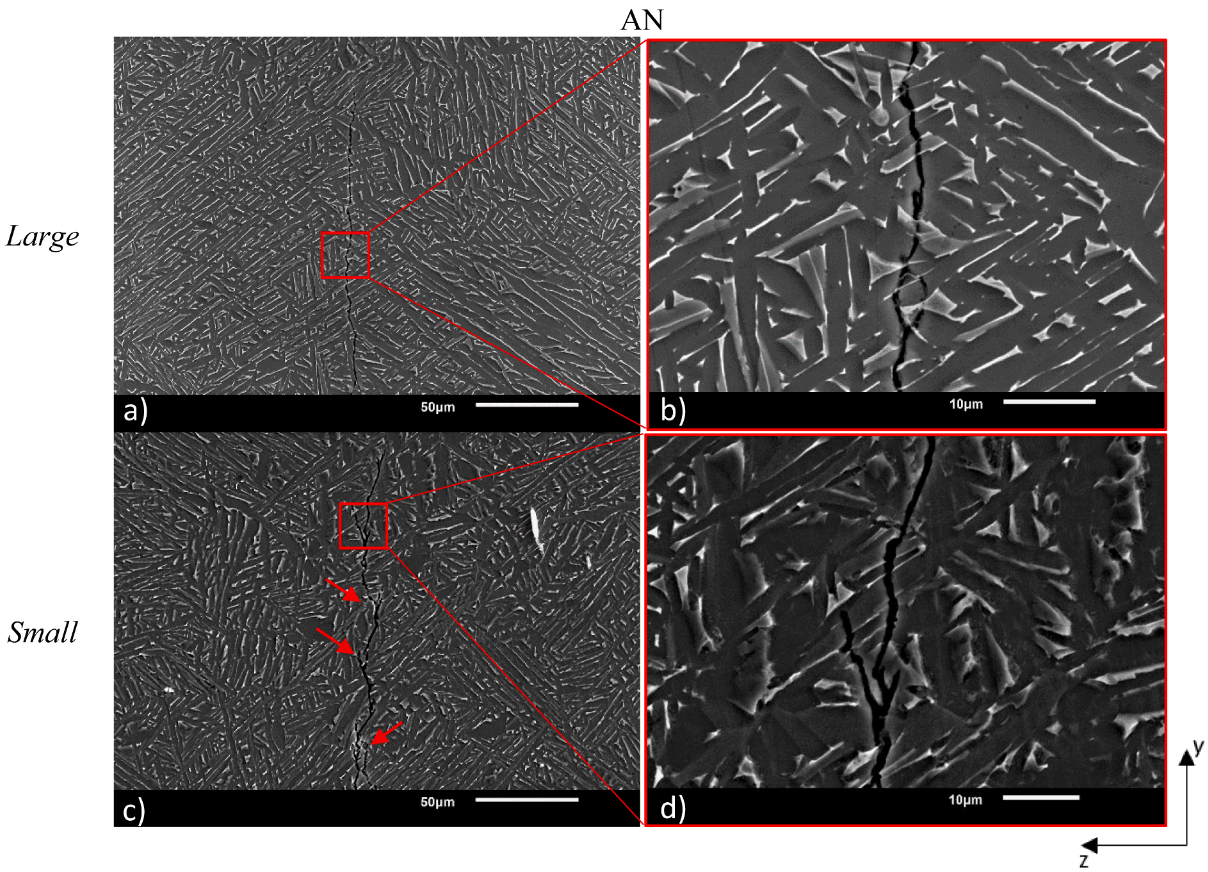

Fig. 6. FCG through AN microstructure in the near threshold regime. With a) & b) large, and c) & d) small specimen groups (b and d presenting respective detailed views.).

sensitive comparatively to the SR microstructure in reducing scales for $\Delta K_{th,eff}$ in LPBF produced Ti-6Al-4 V.

4.2. Size effect on crack tip stress fields

In fracture mechanics-based approaches the value of applied ΔK generated from standard equations compared to effective stress intensity factor range (ΔK_{eff}) experienced by the material is not necessarily equivalent. ΔK_{eff} provides a measure of the effective crack driving force applied in FCG, controlled by the relation $\Delta K_{eff} = K_{max} - K_{op}$, such that K_{op} describes the stress intensity factor at which the crack opens during a loading cycle [57] and growth can occur. The deviation of K_{op} from K_{min} typically is ascribed under the umbrella term of crack closure, where the crack wake makes contact and closes the crack faces prematurely during a loading cycle, effectively retarding the applied ΔK to a lower ΔK_{eff} value. This behaviour has been shown to be highly dependant on R and material flow properties, with lower R values and lower flow stresses leading to more significant closure effects [58,59]. Different attempts have been made to model this behaviour with the Newmans' plasticity formulation commonly used in FCG models [5]. However, with the effect of crack closure subsiding at R > 0.7, any variation between FCG rates of equivalent material is suggested to become negligible [57] and a different explanation is needed. The ΔK_{th} results for the AN material state demonstrate this behaviour, where results vary between the *large* and *small* specimens despite the final R > 0.8 for both groups.

We examine the local ΔK values between *small* and *large* AN specimens as per Section 2.4 and Fig. 8, highlighting the experiential discrepancy between the *small* and *large* AN specimens. A lower measured ΔK is expected at lower R (higher $\Delta K_{applied}$) as crack closure effects become more significant and plasticity-induced crack wake contact shielding is expected to play a larger role in retarding FCG. Furthermore, some deviation is also expected from the method applied outlined in Section 2.4, as the Williams field fitting used literature approximations for E, a plane stress form of bulk modulus and images captured on the specimen surface which is governed by plane stress and not plane strain. However, at higher R > 0.7, in the absence of significant crack closure effects in the crack wake, deviation of the crack driving force found at the crack tip from the standardised equations (and idealised, i.e., under the assumptions of linear elastic fracture mechanics) has been suggested to be from influence of variations in material constraint [60]. The material constraint presents as a term used for describing the three-dimensional effects experienced in the crack front through the thickness of the specimen, which are not inherently described by the simplified two-dimensional plane stress or strain methodologies [61]; higher values of constraint indicate a restriction in plasticity and lower ΔK values [62]. Material constraint may further be split into in-plane and out-of-plane contributions. The latter is associated with specimen thickness, typically compensated for in testing standards through geometry recommendation ratios to meet the plane strain condition and allow the use of governing equations (ASTM E399 [49]). The former is less well defined and has been subject to numerous studies, relating it to specimen geometry, crack length and testing methodology amongst others [62,63]. Subsequently, various parameters have been selected and modelled in attempts to fully describe this feature and its effecting behaviour [62].

Here, first considering the out-of-plane portion of constraint between the *large* and *small* groups suggested to be influenced by specimen thickness (B) and an out-of-plane T-stress component (T_z) [64,65]. Crack front curvature measurements from fracture surfaces show the *large* group for both AN and SR material states exhibit more curved crack fronts of ~ 50–60 % (measured as the difference in length of crack at

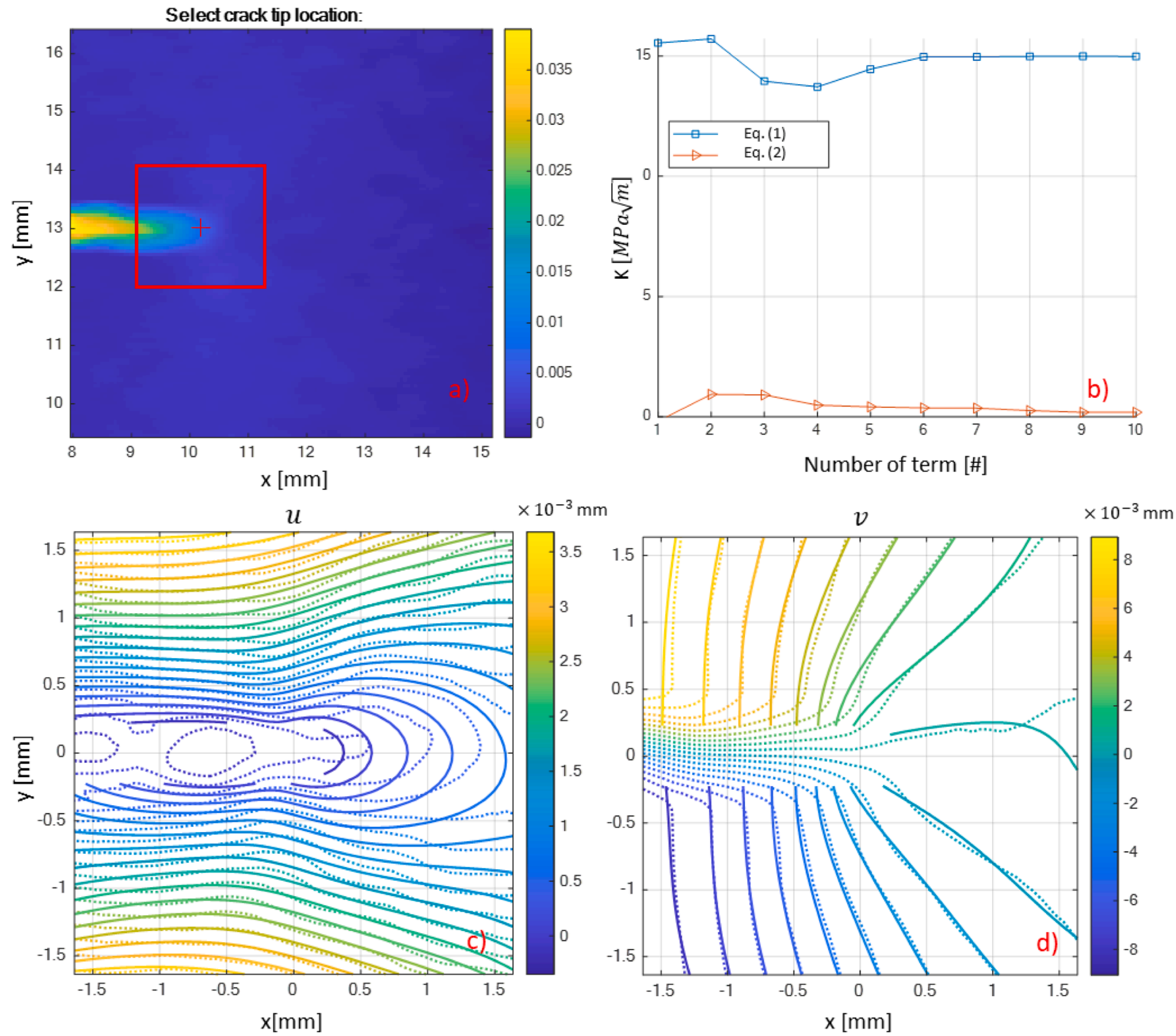

Fig. 7. Schematic of field fitting approach to extract stress intensity factor values, (a) crack tip selection, (b) optimised stress intensity, and (c) & (d) resulting field fits.

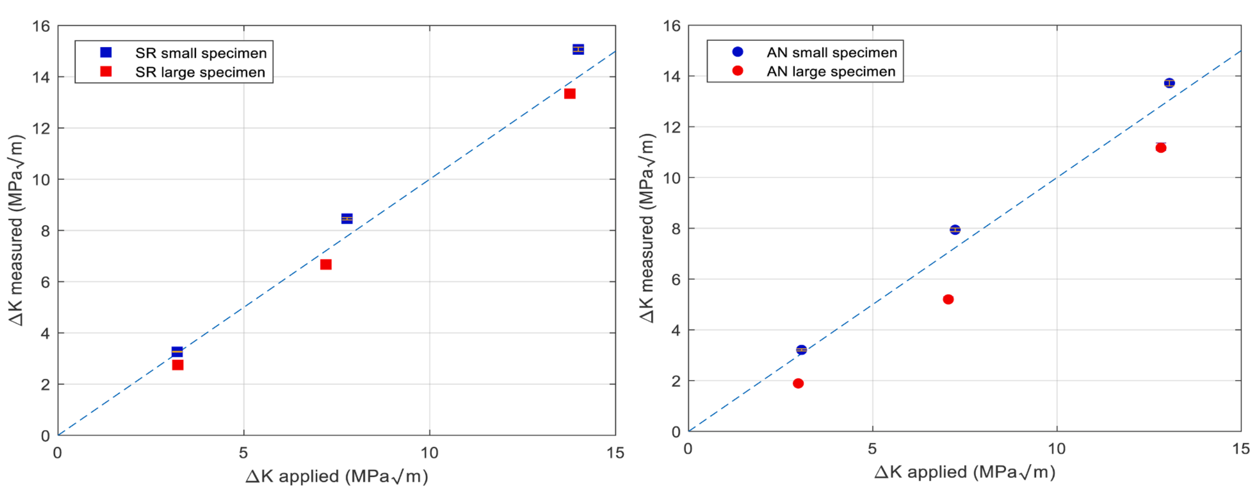

Fig. 8. Fitted stress intensity values for SR and AN material in large and small specimen group.

Table 3
DIC fitted results for specimens in vertical build orientation.

Material State	Group	R	$\Delta K_{applied}$ (MPa$\sqrt{m}$)	$\Delta K_{measured}$ (MPa$\sqrt{m}$)	ΔT-stress (MPa)
SR	*small*	0.1	14.0	15.1 ±0.1	35.8 ±0.6
		0.5	7.78	8.46 ±0.1	19.9 ±0.4
		0.8	3.21	3.26 ±0.1	7.60 ±0.2
	large	0.1	13.8	13.3 ±0.1	12.6 ±0.7
		0.5	7.21	6.67 ±0.1	6.76 ±0.4
		0.8	3.21	2.75 ±0.1	2.12 ±0.2
AN	*small*	0.1	13.1	13.7 ±0.1	20.6 ±0.7
		0.5	7.24	7.94 ±0.1	9.12 ±0.4
		0.8	3.07	3.21 ±0.1	3.80 ±0.4
	large	0.1	12.8	11.2 ±0.2	13.8 ±0.6
		0.5	7.05	5.20 ±0.1	4.44 ±0.3
		0.8	2.98	1.89 ±0.1	1.72 ±0.1

surface and through thickness mid-point presented in Table 4), suggesting a lower degree of out-of-plane constraint in comparison to *small* specimens. However, these variations are once again small and specimen thicknesses are well within limits suggested by the more conservative ASTM E399 standard, therefore the effects of out-of-plane constraint are likely negligible.

Focusing on in-plane constraint, we adopt a non-contact surface measured value of cyclic stress triaxiality (ΔT-stress) as an indicator of constraint [62]. Where this ΔT-stress is proportional to $4{\cdot}a_2$ (Eq. (1)) and simply describes the stress at the crack tip acting parallel to the propagation direction [66]. The ΔT-stress is measured between *large* and *small* groups as a function of $\Delta K_{applied}$. Fig. 10 illustrates this relation with more detail provided in Table 3. Fig. 10 indicates that the ΔT-stress values for *small* specimens in both AN and SR are higher compared to the *large* specimen group. This suggests the value of in-plane constraint at the crack tip for *small* specimens is higher. Which potentially explains the variations in ΔK between the applied and measured, Fig. 8 for AN and suggests a reason the *small* AN present a lower $\Delta K_{th,eff}$ than the large group as illustrated in Fig. 4. Furthermore, a higher effective ΔK than applied would lead to describing the formation of increased bifurcations along the crack path as present in the *small AN* group (Fig. 6). However, this line of thought does not hold for SR, as the difference in ΔT-stress between sizes in SR material is more pronounced than AN, but the measured and applied ΔK values for SR are closer to parity when compared to AN (Fig. 8); and the $\Delta K_{th,eff}$ are similar. Further alluding to the importance of a microstructure-sensitive relation between size reduction and $\Delta K_{th,eff}$, as was discussed in Section 4.1.

Table 4
Crack front curvature.

Material State	Group	Mid-point to surface difference (μm)
SR	*small*	127
	large	254
AN	*small*	169
	large	292

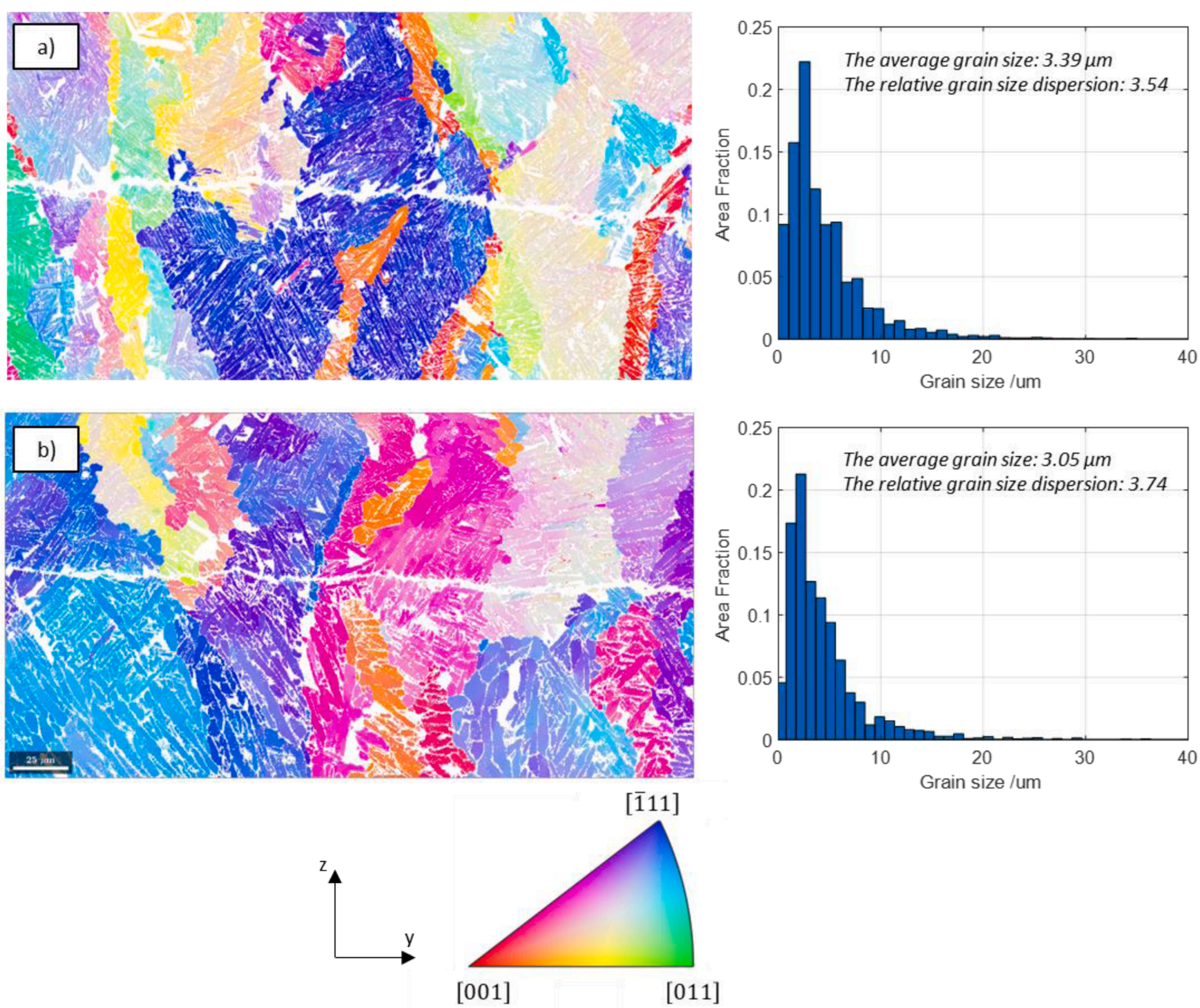

Fig. 9. EBSD crack profile through PBG structure in YZ plane and grain size distribution for AN vertical specimens in the (a) small and (b) large group.

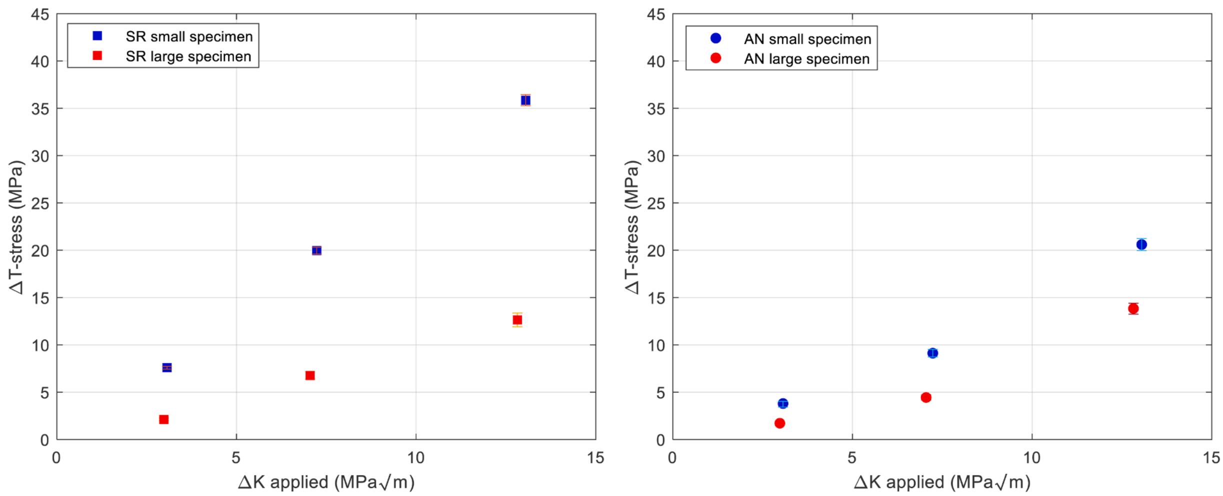

Fig. 10. Fitted ΔT-stress values for SR and AN material in the large and small groups.

We argue that reporting near-threshold FCG behaviour values in LPBF produced Ti-6Al-4 V may benefit from nuance not only in testing methodology and effects of crack closure, but further inclusion of a description of the three-dimensional stress state at the crack tip. In this regard, the material constraint parameter is useful. However, it currently exists as one of many formulations, such as the T-stress, and requires further consolidation and inclusion in existing standardised approximations of ΔK.

4.3. Material constraint as a multiparameter problem

In the light of constraint and microstructural variations the specimen size is but one piece of the puzzle in correctly determining near-threshold behaviour and therefore reliably determining $\Delta K_{th,eff}$ from small scale specimens. Assuming that the small-scale yielding criterion is satisfied and crack closure is negligible at higher loading ratios, we suggest the observed deviation of FCG rates between material states from a mechanical standpoint is due to a difference in material constraint sensitive to both size and microstructure. The previous work of the authors [5] considered collapsing FCG rate data at different R ratios into ΔK_{eff} through Newmans PICC approximation [67], where an arbitrary empirical material constraint parameter is present, and fitted values for different material states varied such that martensitic α' microstructure values of constraint were higher compared to a duplex annealed equiaxed $\alpha+\ \beta$ microstructure [10]. This behaviour was attributed to the relatively higher influence of meso- and microstructure at decreasing ΔKvalues where the plastic zone size governing steady FCG rates decreases towards scales of microstructural features such as grain, α-colony and PBG sizes in LPBF produced Ti-6Al-4 V [5,7,14].

Adopting an energy perspective to describe this difference in constraint, the threshold FCG behaviour is considered for the SR and AN material states. As a result of the work done by the applied load, the energetic state at the crack tip is balanced by the sum of the energy stored at the crack tip used for propagation, elastic work in the active plastic zone, and finally residual strain energy moved into the crack wake [66]. The active plastic zone size in an idealised formulation (i.e. Eq. (3)) suggests the AN r_p is generically larger than SR (~40%) when K_{max} is equivalent, as the value of σ_{ys} is lower. Therefore, the AN material is energetically less constrained around the crack and the amount of total energy from the applied load required for crack propagation is higher. Although Eq. (3) describes the size of the plastic zone as a length ahead of the crack (r_p), including the value of plastic zone size in terms of height perpendicular to propagation is also beneficial from an energy perspective, as it is in the total plastic zone area which consumes energy in the form of elastic work [68]. Sobatka et al. [69] showed that the height of the plastic zone is sensitive to T stress, where increasing the T stress resulted in decreased heights of the plastic zone and wake [69]. This suggests that the higher values of T stress observed in Fig. 10 would lead to less energy dissipation through elastic work and more energy available from the applied load at the crack tip for propagation, therefore a lower $\Delta K_{th,eff}$, as observed for the AN material. Similarly, Ayatollahi et al. [70] used a generalised strain energy density criteria to include the influence of T stress and geometry to estimate FCG rates for a ductile Al 7075-T6 material, suggesting that the inclusion of the non-singular stress term in their energy formulation improved the predictions from experimental results [70]. Conversely, Blason et al. [17] showed good agreement of near-threshold FCG behaviour between standard and small-scale specimens for high strength steel S960QL at R>0.8 without any further modification to experimental ΔK values, which is similar to our observations for SR LPBF produced Ti-6Al-4 V specimens. We postulate that the increase in ΔT-stress can be considered as a form of stiffness increase with reducing plastic wake in the AN material. This behaviour in the SR material is potentially less prevalent and the variation in T-stress caused by geometry is less impactful on resulting $\Delta K_{th,eff}$ values.

In a more familiar fracture mechanics-based approach, Roychowdhury and Dodds [71,72] in lieu of experimental testing adopted a finite element approach including both dimensional thickness B and the effect of T-stress in describing crack growth inhabitation phenomena. In conclusion proposing a two-parameter model as a function of K_{max}, T_{max}, B and σ_{ys} to better describe the finite element generated crack tip stress fields and normalised opening loads K_{op}/K_{max} [71]. The magnitude of the modelled terms reduces in stiffer materials with lower σ_{ys} values, alluding to the more complex relation between microstructural features and the near-threshold FCG behaviour in small scale testing of LPBF produced Ti-6Al-4V.

Typically, the misbehaviour of FCG rates to applied ΔK approximations in standardised testing methodologies is attributed to the crack closure phenomena. However, with interest in deviating from standardised testing toward small-scale testing for AM materials such as LPBF produced Ti-6Al-4V, we argue that including material constraint with nuance for both material geometry and microstructural state is necessary for reliable determination of $\Delta K_{th,\ eff}$ values. To this extent, in the absence of accepted standard practise for small-scale FCG rate testing, advanced characterisation techniques such as DIC are beneficial for validation in accompaniment to standardised testing methodologies in extracting FCG rate properties.

4.4. Sub-size specimen testing considerations

The nature of FCG rate testing of sub-size specimens requires careful consideration in the equipment and testing procedure used. The suitability for its use in $\Delta K_{th,eff}$ determination parallel to damage tolerant models for fatigue prediction is important to consider. In a study on high strength steel Blason et al. [17] highlights required considerations regarding robust testing of FCG rates in the near-threshold regime using sub-size specimens, firstly to maintain the small-scale yielding criterion throughout the test and secondly generate accurate results [17]. As per the standard design of the FCGR testing, the ΔK term is used as measure of crack driving force and empirical derivative for all controlling equations during testing. This requires the small-scale yielding condition to be satisfied of which the remaining crack ligament is descriptive, as per Eq. (4) for SENB specimens (BS 12,108:2018):

$$(W-a) \geq \left(\frac{3\lambda F_{max}}{2B\sigma_{ys}}\right)^{\frac{1}{2}} \tag{4}$$

λ denotes the distance between external support rollers. Therefore, this requirement constrains allowable crack lengths during testing, meaning sub-size specimen with reduced B and material with lower σ_{ys} are more limited in their allowable crack extension range. When Eq. (4) is not satisfied the material around the crack tip enters large scale yielding and the ΔK solutions break down, leading to inaccuracies in the results. While the SSY criteria is typically met when the ratios of specimen size are proportional to those in ASTM and British Standards (BS), this constraint becomes significant in combination with the requirements of the pre-crack ($\sim$1 mm for $W = 5$ mm) and amount of crack extension required to determine sufficient measurement points for describing the near-threshold behaviour [17]. Furthermore, for smaller specimens this requirement strains the selection of loadshedding gradients, where we selected a value -0.095 m^{-1} whereas ASTM E647 [30] recommends a gradient of -0.08 m^{-1}. This may affect smaller specimens and softer materials, however the constant K_{max} type testing used has the benefit of constant r_p size ahead of the crack tip throughout the test, $\sim$ 10 and 14 μm for SR and AN material in this work. Comparatively, load reduction steps were performed at crack extensions of 100 μm therefore load history effects are minimised and the effect of the small increase in gradient used is unlikely to affect the results [73].

The second important consideration is the sensitivity of the crack monitoring technique to the size and material of the specimens. The DCPD technique is considered sufficiently accurate for FCG rate testing as the method typically has a higher resolution capable of resolving smaller crack increments, when compared to CTOD and visual measurements [17]. However, as the FCG approaches threshold, the required resolution of the potential difference increase required to describe crack growth in the 10^{-7} to 10^{-8} mm/cycle decade increases, which, in combination with the natural noise induced by the setup, results in a greater degree of scatter in data, making the post-processing step more integral and reporting of $\Delta K_{th,eff}$ in ranges more realistic. This observation, in combination with the limited material available in sub-size specimens, suggests reducing the scale of FCG rate testing requires nuance in application of methodologies, suitable equipment and better description of data post-processing standards to ensure repeatability between applications and realistic results.

From a holistic perspective, the aforementioned testing constraints and micro-structural sensitive results from this work suggest there are still open questions regarding the suitability of sub-size specimens for $\Delta K_{th,eff}$ determination and use in frameworks such as damage-tolerant fatigue predictions, where the fatigue strength estimation in the high cycle regime is suggested to be sensitive to the values of $\Delta K_{th,eff}$ and R-dependant $\Delta K_{th,lc}$ respectively [10]. Furthermore, the values of $\Delta K_{th,eff}$ and $\Delta K_{th,lc}$ are linked, demonstrated in previous work by the authors where the capability of collapsing $\Delta K_{th,lc}$ for a range of R values into a singular material specific $\Delta K_{th,eff}$ value through description of crack closure effects is effectively demonstrated [5]. This relation suggests any discrepancy between sub-size and standard specimen $\Delta K_{th,eff}$ values, as in the AN material state, would further limit such methodologies in reliably describing a range of loading conditions for full scale parts.

Nevertheless, arguably sub-size specimen testing remains a promising avenue of testing in LPBF produced builds, as demonstrated by the parity for the SR material and two orientations tested, and notable feasibility of near threshold FCG testing on sub-size specimens of high strength steel S960QL presented by Blason et al. [17]. While the discussions here are limited to a perspective on the scale order of multiple grains, and ΔK and plasticity approximations around the crack tip, the effect of microstructures in LPBF produced Ti-6Al-4 V in lower order scales may be necessary to understand and further sub-size specimen testing for reliable $\Delta K_{th,eff}$ determination.

5. Concluding remarks

The $\Delta K_{th,eff}$ parameter is an important parameter for fracture mechanics-based damage tolerant fatigue prediction models [10], where for LPBF produced Ti-6Al-4 V builds fatigue strength approximations are sensitive to these values. The use of sub-size specimen testing to accompanying full scale LPBF produced Ti-6Al-4 V builds is an attractive solution to further qualification and certification of builds on a build-by-build basis, without foregoing the benefit inherent to AM techniques. This work discusses the current suitability of using small scale specimens alongside AM builds, finding reliable implementation infeasible without first understanding key behaviours at a reduced specimen size. Namely,

- $\Delta K_{th,eff}$ values determined from sub-size specimens for LPBF produced Ti-6Al-4 V are inconsistent for different microstructures, where the AN material presented here illustrated a decreased FCG resistance at the reduced size.
- Reducing specimen size influences both in- and out-of-plane crack tip constraint, with notable increase of in-plane constraint values for smaller specimens.
- Practically, standardised testing methods and equipment are not designed for sub-size specimens, meaning validity of existing crack monitoring techniques and testing designs need to be carefully considered for accurately determine $\Delta K_{th,eff}$ values.

The link between specimen size, constraint and microstructure for LPBF produced Ti-6Al-4 V as specimen size reduces is unclear. Where sub-size AN specimens demonstrate a sensitivity to reduction in size and variation in material constraint, SR material is evidently unaffected and not all explanations insofar as the size effect hold true for both material states. While this work offers insight towards the establishing this link between combined features and near-threshold behaviour, a greater depth of understanding is required before reliable sub- size specimens should be used in an AM certification framework.

Declaration of Competing Interest

The authors declare that they have no known competing financial interests or personal relationships that could have appeared to influence the work reported in this paper.

Acknowledgments

The authors are grateful to the Department of Science and Innovation through the Collaborative Program for Additive Manufacturing (CPAM) administered by the Council for Scientific and Industrial Research (CSIR) for the project funding, through contract number S004063. Material Science and Engineering (MSE) department of Delft University of

Technology (TUD) is acknowledged for supporting mechanical tests and microstructural characterization. Finally, the Electron Microscope Unit, University of Cape Town for EBSD support.

References

[1] T.H. Becker, P. Kumar, U. Ramamurty, Fracture and fatigue in additively manufactured metals, Acta Mater. 219 (2021), https://doi.org/10.1016/j.actamat.2021.117240. Acta Materialia IncOct. 15.
[2] S. Williams, F. Martina, D. Wood, A. Garcia Colomo, A comparison framework to support the selection of the best additive manufacturing process for specific aerospace applications, Int. J. Rapid Manuf. 9 (3) (2020) 1, https://doi.org/10.1504/ijrapidm.2020.10019230.
[3] P. Kumar, U. Ramamurty, High cycle fatigue in selective laser melted Ti-6Al-4V, Acta Mater. 194 (2020) 305–320, https://doi.org/10.1016/j.actamat.2020.05.041. Aug.
[4] S.M. Ahmadi, et al., From microstructural design to surface engineering: a tailored approach for improving fatigue life of additively manufactured meta-biomaterials, Acta Biomater. 83 (2019) 153–166, https://doi.org/10.1016/j.actbio.2018.10.043. Jan.
[5] N. Macallister, K. Vanmeensel, T.H. Becker, Fatigue crack growth parameters of laser powder bed fusion produced Ti-6Al-4V, Int. J. Fatigue 145 (2021), https://doi.org/10.1016/j.ijfatigue.2020.106100. Apr.
[6] G.M. Ter Haar, T.H. Becker, Selective laser melting produced Ti-6Al-4V: post-process heat treatments to achieve superior tensile properties, Materials 11 (1) (2018), https://doi.org/10.3390/ma11010146. Jan.
[7] P. Kumar, O. Prakash, U. Ramamurty, Micro-and meso-structures and their influence on mechanical properties of selectively laser melted Ti-6Al-4V, Acta Mater. 154 (2018) 246–260, https://doi.org/10.1016/j.actamat.2018.05.044. Aug.
[8] K. Karami, et al., Continuous and pulsed selective laser melting of Ti6Al4V lattice structures: effect of post-processing on microstructural anisotropy and fatigue behaviour, Addit. Manuf. 36 (2020), https://doi.org/10.1016/j.addma.2020.101433. Dec.
[9] S. Romano, A. Brandão, J. Gumpinger, M. Gschweitl, S. Beretta, Qualification of AM parts: extreme value statistics applied to tomographic measurements, Mater. Des. 131 (2017) 32–48, https://doi.org/10.1016/j.matdes.2017.05.091. Oct.
[10] N. Macallister, T.H. Becker, Fatigue life estimation of additively manufactured Ti-6Al-4V: sensitivity, scatter and defect description in damage-tolerant models, Acta Mater. 237 (2022), https://doi.org/10.1016/j.actamat.2022.118189. Sep.
[11] J. Maierhofer, H.P. Gänser, R. Pippan, Modified Kitagawa-Takahashi diagram accounting for finite notch depths, Int. J. Fatigue 70 (2015) 503–509, https://doi.org/10.1016/j.ijfatigue.2014.07.007.
[12] U. Zerbst, et al., Damage tolerant design of additively manufactured metallic components subjected to cyclic loading: state of the art and challenges, Prog. Mater Sci. 121 (2021), https://doi.org/10.1016/j.pmatsci.2021.100786. Elsevier LtdAug. 01.
[13] H. Döker, Fatigue crack growth threshold: implications, determination and data evaluation, Int. J. Fatigue 19 (93) 145149, doi:10.1016/s0142-1123(97)00058-3.
[14] P. Kumar, U. Ramamurty, Microstructural optimization through heat treatment for enhancing the fracture toughness and fatigue crack growth resistance of selective laser melted Ti–6Al–4V alloy, Acta Mater. 169 (2019) 45–59, https://doi.org/10.1016/j.actamat.2019.03.003. May.
[15] R. Pippan, A. Hohenwarter, Fatigue crack closure: a review of the physical phenomena, in: Fatigue and Fracture of Engineering Materials and Structures, 40, Blackwell Publishing Ltd, 2017, pp. 471–495, https://doi.org/10.1111/ffe.12578. Apr. 01.
[16] G.E. Lucas, The development of small specimen mechanical test techniques, J. Nucl. Mater. 117 327339, doi:10.1016/0022-3115(83)90041-7.
[17] S. Blasón, et al., Determination of fatigue crack growth in the near-threshold regime using small-scale specimens, Theor. Appl. Fract. Mech. 118 (2022), https://doi.org/10.1016/j.tafmec.2021.103224. Apr.
[18] R.J. Lancaster, S.P. Jeffs, H.W. Illsley, C. Argyrakis, R.C. Hurst, G.J. Baxter, Development of a novel methodology to study fatigue properties using the small punch test, Mater. Sci. Eng. A 748 (2019) 21–29, https://doi.org/10.1016/j.msea.2019.01.074. Mar.
[19] NASA Standard, MSFC-STD-3716, Standard for additively manufactured spaceflight hardware by laser powder bed fusion in metals, 2017.
[20] H. Liu, Y. Shen, S. Yang, P. Zheng, L. Zhang, A comprehensive solution to miniaturized tensile testing: specimen geometry optimization and extraction of constitutive behaviors using inverse FEM procedure, Fusion Eng. Des. 121 (2017) 188–197, https://doi.org/10.1016/j.fusengdes.2017.07.016. Oct.
[21] F. Chen, S. Chen, X.H. Dong, C.Y. Li, X.T. Hong, X.P. Zhang, Size effects on tensile strength of aluminum-bronze alloy at room temperature, Mater. Des. 85 (2015) 778–784, https://doi.org/10.1016/j.matdes.2015.06.169. Nov.
[22] . Kohno,et, et al., Specimen size effects on the tensile properties of JPCA and JFMS, J. Nucl. Mater. 283287 10141017, doi:10.1016/s0022-3115(00)00245-2.
[23] J. Dzugan, et al., Effects of thickness and orientation on the small scale fracture behaviour of additively manufactured Ti-6Al-4V, Mater. Charact. 143 (2018) 94–109, https://doi.org/10.1016/j.matchar.2018.04.003. Sep.
[24] ASTM, F3001-14, Standard specification for additive manufacturing titanium-6 aluminum-4 vanadium ELI (extra low interstitial) with powder bed fusion , doi: 10.1520/F3001-14R21.
[25] F. Niessen, T. Nyyssönen, A.A. Gazder, R. Hielscher, Parent grain reconstruction from partially or fully transformed microstructures in MTEX, J. Appl. Crystallogr. 55 (2022) 180–194, https://doi.org/10.1107/S1600576721011560. Feb.
[26] P. Lehto, J. Romanoff, H. Remes, T. Sarikka, Characterisation of local grain size variation of welded structural steel, Weld. World 60 (4) (2016) 673–688, https://doi.org/10.1007/s40194-016-0318-8. Jul.
[27] P. Lehto, H. Remes, T. Saukkonen, H. Hänninen, J. Romanoff, Influence of grain size distribution on the Hall-Petch relationship of welded structural steel, Mater. Sci. Eng. A 592 (2014) 28–39, https://doi.org/10.1016/j.msea.2013.10.094. Jan.
[28] S. Ghorbanpour, et al., Effect of microstructure induced anisotropy on fatigue behaviour of functionally graded Inconel 718 fabricated by additive manufacturing, Mater. Charact. 179 (2021), https://doi.org/10.1016/j.matchar.2021.111350. Sep.
[29] S. Ghorbanpour, et al., Additive manufacturing of functionally graded inconel 718: effect of heat treatment and building orientation on microstructure and fatigue behaviour, J. Mater. Process. Technol. 306 (2022), https://doi.org/10.1016/j.jmatprotec.2022.117573. Aug.
[30] ASTM. E647-15, Standard test method for measurement of fatigue crack growth rates, 2015, https://doi.org/10.1520/E0647.
[31] M.L. Williams, C. Pasadena, On the Stress Distribution at the Base of a Stationary Crack, Journal of Applied Mechanics 24 109-114, doi:10.1115/1.4011454.
[32] R. Bigger, et al.. A good practices guide for digital image correlation, 2018, https://doi.org/10.32720/idics/gpg.ed1.
[33] J.R. Yates, M. Zanganeh, Y.H. Tai, Quantifying crack tip displacement fields with DIC, Eng. Fract. Mech. 77 (11) (2010) 2063–2076, https://doi.org/10.1016/j.engfracmech.2010.03.025. Jul.
[34] G.M. Ter Haar, T.H. Becker, D.C. Blaine, Influence of heat treatments on the microstructure and tensile behaviour of selective laser melting-produced TI-6AL-4V parts, S. Afr. J. Ind. Eng. 27 (3SpecialIssue) (2016) 174–183, https://doi.org/10.7166/27-3-1663.
[35] P. Miarka, A.S. Cruces, S. Seitl, L. Malíková, P. Lopez-Crespo, Influence of the constraint effect on the fatigue crack growth rate in S355 J2 steel using digital image correlation, Fatigue Fract. Eng. Mater. Struct. 43 (8) (2020) 1703–1718, https://doi.org/10.1111/ffe.13198. Aug.
[36] S. Yoneyama, T. Ogawa, Y. Kobayashi, Evaluating mixed-mode stress intensity factors from full-field displacement fields obtained by optical methods, Eng. Fract. Mech. 74 (9) (2007) 1399–1412, https://doi.org/10.1016/j.engfracmech.2006.08.004. Jun.
[37] R. Harilal, C.P. Vyasarayani, M. Ramji, A linear least squares approach for evaluation of crack tip stress field parameters using DIC, Opt. Lasers Eng. 75 (2015) 95–102, https://doi.org/10.1016/j.optlaseng.2015.07.004. Jul.
[38] M.R. Ayatollahi, M. Nejati, An over-deterministic method for calculation of coefficients of crack tip asymptotic field from finite element analysis, Fatigue Fract. Eng. Mater. Struct. 34 (3) (2011) 159–176, https://doi.org/10.1111/j.1460-2695.2010.01504.x. Mar.
[39] O.N. Belova, L.V. Stepanova, Importance of the higher order terms of the Williams series expansion: experimental aspects and finite element simulations. Procedia Structural Integrity, Elsevier B.V., 2021, pp. 770–785, https://doi.org/10.1016/j.prostr.2022.03.151.
[40] J.W. Pegues, et al., Fatigue of additive manufactured Ti-6Al-4V, part I: the effects of powder feedstock, manufacturing, and post-process conditions on the resulting microstructure and defects, Int. J. Fatigue 132 (2020), https://doi.org/10.1016/j.ijfatigue.2019.105358. Mar.
[41] L. Facchini, E. Magalini, P. Robotti, A. Molinari, S. Höges, K. Wissenbach, Ductility of a Ti-6Al-4V alloy produced by selective laser melting of prealloyed powders, Rapid Prototyp. J. 16 (6) (2010) 450–459, https://doi.org/10.1108/13552541011083371.
[42] N. Davari, A. Rostami, S.M. Abbasi, Effects of annealing temperature and quenching medium on microstructure, mechanical properties as well as fatigue behavior of Ti-6Al-4V alloy, Mater. Sci. Eng. A 683 (2017) 1–8, https://doi.org/10.1016/j.msea.2016.11.095. Jan.
[43] T. Yuri, Y. Ono, T. Ogata, H. Sunakawa, Effect of microstructure on high-cycle fatigue properties of Ti-6Al-4V alloy forging at cryogenic temperatures, in: Proceedings of the AIP Conference Proceedings, American Institute of Physics Inc., 2014, pp. 27–33, https://doi.org/10.1063/1.4860600.
[44] J. Yang, H. Yu, J. Yin, M. Gao, Z. Wang, X. Zeng, Formation and control of martensite in Ti-6Al-4V alloy produced by selective laser melting, Mater. Des. 108 (2016) 308–318, https://doi.org/10.1016/j.matdes.2016.06.117. Oct.
[45] J. Zheng, H. Liu, Y. Ren, L. Zhu, Effect of two-dimensional ultrasonic rolling on grain size and micro-hardness of 7075 aluminum alloy, Int. J. Adv. Manuf. Technol. 106 (1–2) (2020) 503–510, https://doi.org/10.1007/s00170-019-04640-y. Jan.
[46] V. Cain, L. Thijs, J. van Humbeeck, B. van Hooreweder, R. Knutsen, Crack propagation and fracture toughness of Ti6Al4V alloy produced by selective laser melting, Addit. Manuf. 5 (2015) 68–76, https://doi.org/10.1016/j.addma.2014.12.006. Jan.
[47] T.H. Becker, N.M. Dhansay, G.M. ter Haar, K. Vanmeensel, Near-threshold fatigue crack growth rates of laser powder bed fusion produced Ti-Aal-4V, Acta Mater. 197 (2020) 269–282, https://doi.org/10.1016/j.actamat.2020.07.049. Sep.
[48] J. Su, et al., Phase transformation mechanisms, microstructural characteristics and mechanical performances of an additively manufactured Ti-6Al-4V alloy under dual-stage heat treatment, Mater. Des. 223 (2022), https://doi.org/10.1016/j.matdes.2022.111240. Nov.
[49] ASTM, E399-17, Standard Test Method for Linear-Elastic Plane-Strain Fracture Toughness KIc of Metallic Materials, doi:10.1520/E0399-17.

[50] M.R. Molteno, T.H. Becker, Mode I-III decomposition of the j-integral from DIC displacement data, Strain 51 (6) (2015) 492–503, https://doi.org/10.1111/str.12166. Dec.

[51] S. Suresh, Fatigue of Materials, 2nd ed., Cambridge University Press, Cambridge, 1998 https://doi.org/10.1017/CBO9780511806575.

[52] D. Kujawski, F. Ellyin, On the size of plastic zone ahead of crack tip, Eng. Fract. Mech. 25 (2) (1986) 229–236, https://doi.org/10.1016/0013-7944(86)90219-5.

[53] K. Sadananda, D.N.V. Ramaswamy, Role of crack tip plasticity in fatigue crack growth, Philos. Mag. A Phys. Condens. Matter Struct. Defects Mech. Prop. 81 (5) (2001) 1283–1303, https://doi.org/10.1080/01418610108214441.

[54] S.M.J. Razavi, B. van Hooreweder, F. Berto, Effect of build thickness and geometry on quasi-static and fatigue behavior of Ti-6Al-4V produced by electron beam melting, Addit. Manuf. 36 (2020), https://doi.org/10.1016/j.addma.2020.101426. Dec.

[55] B. Vrancken, L. Thijs, J.P. Kruth, J. van Humbeeck, Heat treatment of Ti6Al4V produced by selective laser melting: microstructure and mechanical properties, J. Alloys Compd. 541 (2012) 177–185, https://doi.org/10.1016/j.jallcom.2012.07.022. Nov.

[56] J.T. Burns, J. Boselli, Effect of plate thickness on the environmental fatigue crack growth behavior of AA7085-T7451, Int. J. Fatigue 83 (2016) 253–268, https://doi.org/10.1016/j.ijfatigue.2015.10.020. Feb.

[57] A.K. Vasudevan, D. Kujawski, Analyses of KOP relationship to threshold Kmax,th, Eng. Fract. Mech. 245 (2021), https://doi.org/10.1016/j.engfracmech.2021.107561. Mar.

[58] A.K. Vasudeven, K. Sadananda, N. Louat, A review of crack closure, fatigue crack threshold and related phenomena, Mater. Sci. Eng. A 188 (12) 122, doi:10.1016/0921-5093(94)90351-4.

[59] D. Kujawski, Enhanced model of partial crack closure for correlation of R-ratio effects in aluminum alloys, Int. J. Fatigue 23 (2) 95102, doi:10.1016/s0142-1123(00)00085-2.

[60] J.Y. Xu, G.Z. Wang, F.Z. Xuan, S.T. Tu, Unified constraint parameter based on crack-tip opening displacement, Eng. Fract. Mech. 200 (2018) 175–188, https://doi.org/10.1016/j.engfracmech.2018.07.021. Sep.

[61] F. Yusof, Three-dimensional assessments of crack tip constraint, Theor. Appl. Fract. Mech. 101 (2019) 1–16, https://doi.org/10.1016/j.tafmec.2019.01.025. Jun.

[62] X. Huang, Y. Liu, X. Huang, New constraint parameters based on crack tip plastic zone: theoretical derivations and effectiveness verification, Int. J. Solids Struct. 190 (2020) 129–147, https://doi.org/10.1016/j.ijsolstr.2019.11.009. May.

[63] J. Hebel, J. Hohe, V. Friedmann, D. Siegele, Experimental and numerical analysis of in-plane and out-of-plane crack tip constraint characterization by secondary fracture parameters, Int. J. Fract. 146 (3) (2007) 173–188, https://doi.org/10.1007/s10704-007-9160-8. Aug.

[64] W. Guo, Elastoplastic three dimensional crack border field—II. asymptotic solution for the field, Eng. Fract. Mech. 46 (1) (1993) 105–113, https://doi.org/10.1016/0013-7944(93)90307-E.

[65] W. Guo, Elastoplastic three dimensional crack border field—I. singular structure of the field, Eng. Fract. Mech. 46 (1) (1993) 93–104, https://doi.org/10.1016/0013-7944(93)90306-D.

[66] M. Gupta, R.C. Alderliesten, R. Benedictus, A review of T-stress and its effects in fracture mechanics, Eng. Fract. Mech. 134 (2015) 218–241, https://doi.org/10.1016/j.engfracmech.2014.10.013. Jan. 01.

[67] J.C. Newman Jr., A crack-closure model for predicting fatigue crack growth under aircraft spectrum loading, ASTM Special Technical Publication 748 (1981) 53–84, https://doi.org/10.1520/STP28334S.

[68] A.G. Varias, C.F. Shih, Quasi-static crack advance under a range of constraints—steady-state fields based on a characteristic length, J. Mech. Phys. Solids 41 (5) (1993) 835–861, https://doi.org/10.1016/0022-5096(93)90002-W.

[69] J.C. Sobotka, R.H. Dodds, T-stress effects on steady crack growth in a thin, ductile plate under small-scale yielding conditions: three-dimensional modeling, Eng. Fract. Mech. 78 (6) (2011) 1182–1200, https://doi.org/10.1016/j.engfracmech.2010.11.018. Apr.

[70] M.R. Ayatollahi, M.R. Moghaddam, F. Berto, T-stress effects on fatigue crack growth – theory and experiment, Eng. Fract. Mech. 187 (2018) 103–114, https://doi.org/10.1016/j.engfracmech.2017.10.025. Jan.

[71] S. Roychowdhury, R.H. Dodds, Effect of T-stress on fatigue crack closure in 3-D small-scale yielding, Int. J. Solids Struct. 41 (9–10) (2004) 2581–2606, https://doi.org/10.1016/j.ijsolstr.2003.11.004. May.

[72] S. Roychowdhury, R.H. Dodds, Three-dimensional effects on fatigue crack closure in the small-scale yielding regime a finite element study, Fatigue. Fract. Eng. Mater. Struct. 26 663673, doi:10.1046/j.1460-2695.2003.00655.x.

[73] Y. Yamada, J.C. Newman, Crack closure under high load ratio and Kmax test conditions, in: Proceedings of the Procedia Engineering, 2010, pp. 71–82, https://doi.org/10.1016/j.proeng.2010.03.008. Apr.